JOURNAL OF THE AMERICAN CHEMICAL SOCIETY
pubs.acs.org/JACS
Article

Atomically Precise $[Cu_{23}H_4(SC_7H_7)_{18}(PPh_3)_6]$ Nanocluster: Structural Integration of Johnson Solids through a Cu(0) Center and Electrocatalytic Functionality

Sourav Biswas,○ Yamato Shingyouchi,○ Maho Kamiyama, Masaki Ogami, Haohong Song, Bo Li, Song Wang, Tokuhisa Kawawaki,* De-en Jiang,* and Yuichi Negishi*

Cite This: J. Am. Chem. Soc. 2025, 147, 23733−23742

Read Online

ACCESS | Metrics & More | Article Recommendations | Supporting Information

ABSTRACT: In recent years, copper (Cu) nanoclusters (NCs) have attracted significant attention for their potential in catalytic applications. However, the inherent high reactivity of Cu(0) often leads to instability, making it challenging to synthesize stable Cu(0)-based NCs. As a result, most reported systems are limited to Cu(I)-based NCs, which in turn constrains their effectiveness and broader applicability in catalysis. Here, we present a synthetic strategy to fabricate a stable Cu(0)-containing, $[Cu_{23}H_4(SC_7H_7)_{18}(PPh_3)_6]$ NC, where the Cu(0) center is atomically protected by two Cu(I)-based Johnson solids and stabilized by the additional Cu(I) units, thiolate ligands and interstitial hydrides. Although neutral PPh_3 ligands are also present, their attachment is positioned away from the Cu(0) center, primarily serving to stabilize the overall geometry and prevent further structural distortions. This robust architectural framework enables the NC to maintain exceptional structural stability and catalytic performance in electrochemical CO_2 reduction reactions, facilitating a consistent selectivity for the end product over time. Density functional theory calculations validate the experimental findings, confirming HCOOH as the preferred product. This preference arises from the lower limiting potential for *HCOO formation, attributed to its enhanced stabilization through a favorable combination of electronic and geometric structure—features that clearly distinguish it from Cu(I) NCs.

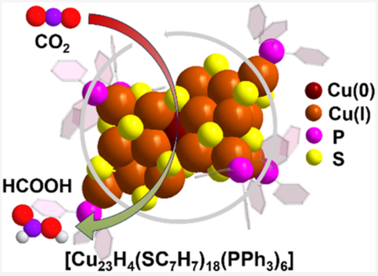

INTRODUCTION

Leveraging the nm-scale size regime and discrete electronic structure, atomically precise metal nanoclusters (NCs) have rapidly emerged as a significant area of interest in materials chemistry research.[1,2] Initially, the focus was predominantly on noble metals, such as gold (Au) and silver (Ag), due to their favorable properties and relative ease of synthesis.[3−6] However, recent advancements in synthetic methods have expanded the scope of metal NCs to include elements from the first row of the transition metals.[7] The synthesis of these first-row transition metal NCs presents unique challenges, particularly regarding their stability.[8−10] These NCs often exhibit higher reactivity, making them more prone to degradation or transformation, a characteristic that has historically limited their practical applications. Nonetheless, with improved control over reaction conditions and a deeper understanding of the factors influencing stability, researchers have been able to produce several types of stable first-row transition metal NCs. These advancements have not only demonstrated that stability concerns can be mitigated but also opened up new avenues for exploring the applications of these NCs. Among these, Cu NCs have emerged rapidly due to their favorable catalytic properties.[11−19]

On the otherhand, the electrochemical reduction of carbon dioxide (CO_2) has gained considerable attention for its potential to tackle both environmental and energy issues.[20−24] Catalysts are essential for increasing the efficiency and selectivity of this reaction, thereby making it more feasible for large-scale implementation. Among the various catalysts studied for this purpose, NC-based catalysts stand out due to their small size, discrete nature and distinctive electronic properties.[25] Although copper (Cu) NCs are relatively new compared to their Au and Ag counterparts, they exhibit unique binding affinities with CO_2 and its reductive intermediates, facilitating the reduction process with a range of end products.[26−30]

Although the beneficial effects of Cu NCs as catalysts are well-recognized, their limited availability and stability hinder their broader utilization in selective end-product catalytic reactions. To date, only a small number of Cu NCs have been identified and used as electrocatalysts for reduction reactions.[30−32] Most of these NCs contain only a few Cu atoms, where the geometric architecture influences the selectivity of the resulting end products.[33−38] For high-nuclearity Cu NCs,

Received: April 3, 2025
Revised: June 17, 2025
Accepted: June 18, 2025
Published: June 26, 2025

https://doi.org/10.1021/jacs.5c05665
J. Am. Chem. Soc. 2025, 147, 23733−23742

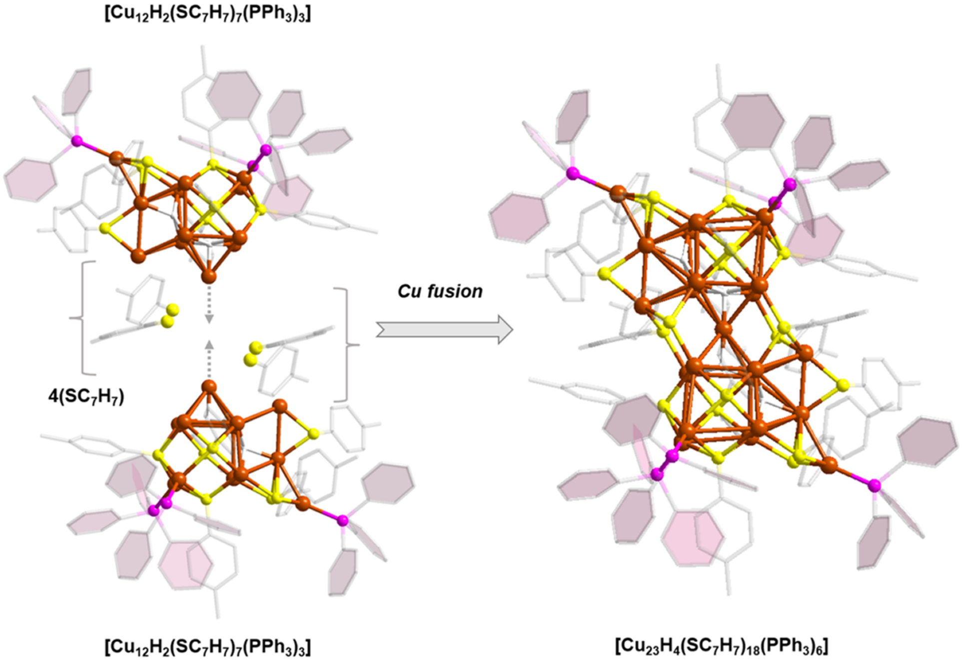

Figure 1. Overall structural architecture of Cu_{23} NC which is formed by fusion of two identical Cu subunits through a Cu atom. Hydrogen atoms are removed from the ligands for clarity. Color legend: Cu, brown; S, yellow; P, violet; H, white; and C, gray stick. Benzene rings of PPh_3 units are filled with color for easy differentiation.

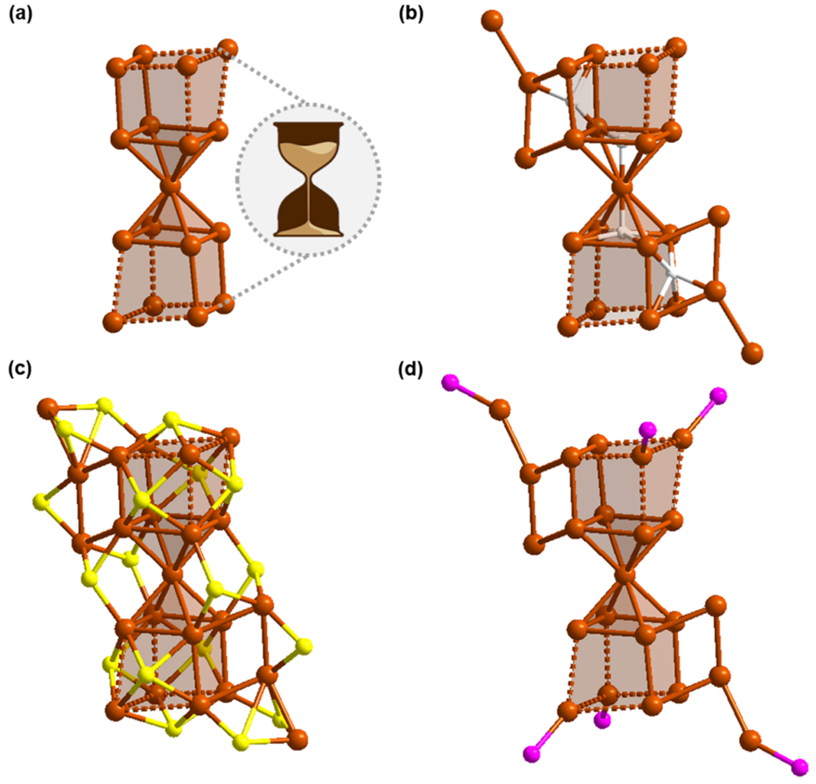

Figure 2. (a) Bielongated square pyramidal geometry of fused Cu_{17} which resembles a sand timer, (b) attachment of additional Cu_3 units and the location of the hydrides inside the NC unit, (c) attachment of the thiolate ligands on the NC unit, and (d) attachment of PPh_3 ligand on the NC unit. All the carbon parts and associated hydrogen atoms are removed for the clarity. Color legend: Cu, brown; S, yellow; P, violet; H, white.

lattice hydrides play a crucial role in shaping mechanistic pathways and determining product selectivity.[39−42] However, there is a limited number of studies exploring the catalytic role of high-nuclearity Cu NCs containing interstitial hydrides. Therefore, there is a valuable opportunity to explore how this structural architecture affects the selectivity of different end products. Another significant concern is the oxidation state of the metal atoms within these NCs. The literature indicates that Cu(I) is predominantly present in the structure of Cu NCs used for CO_2 reduction reactions (CO_2RR).[30] There is a notable scarcity of Cu(0)-containing NCs due to their high reactivity, which makes their stabilization and utilization as catalysts during electrochemical processes particularly challenging. Thus, the presence of Cu(0) in the structure of Cu NCs thus presents additional difficulties in employing them as effective catalysts.[43−45]

In the view of the above-mentioned facts, here we synthesized $[Cu_{23}H_4(SC_7H_7)_{18}(PPh_3)_6]$ (Cu_{23}) NC (SC_7H_7: *p*-toluenethiolate) which is constructed by the fusion of two identical geometric solids through a Cu(0) center. The distinctive geometric architecture of this NC ensures high stability, even with the presence of Cu(0), and allows it to be successfully loaded onto the carbon black (CB) surface without altering its electronic structure, enabling its use as an effective electrochemical catalyst. During the electrochemical process it shows a high selectivity for formic acid (HCOOH) formation and density functional theory (DFT) calculations further confirm the selectivity by identifying the active catalytic site and elucidating the CO_2 reduction mechanism.

■ RESULTS AND DISCUSSION

The synthesis of Cu_{23} NC was carried out using a $[BH_4]^-$ reduction approach. Initially, the $[Cu(CH_3CN)_4BF_4]$ precursor was treated with PPh_3 and *p*-toluenethiol in a mixture of acetonitrile and chloroform. Reduction was then achieved by adding methanolic solution of $NaBH_4$ in ice cold condition. The final product was extracted in chloroform, from which yellow, rod-shaped crystals were obtained through liquid−liquid diffusion with *n*-hexane. The detail synthetic process is explained in Supporting Information file. Single crystal X-ray diffraction (SCXRD) analysis provided detailed structural insights of the obtained crystals. The results reveal that this NC crystallizes within a triclinic crystal system, specifically adopting the space group *P*-1 (No. 2) (Table S1). A thorough structural analysis reveals an unconventional arrangement of Cu atoms and ligands, highlighting a configuration that departs from the typical core−shell architecture. Rather than forming a single-core structure, this NC is composed of two fused $[Cu_{12}H_2(SC_7H_7)_7(PPh_3)_3]$ subunits, resulting in a distinctive dimeric assembly (Figure 1). This fusion process is mediated by the strategic sharing of a single Cu atom positioned at a vertex, along with four additional thiolate ligands, between the two subunits. Nine Cu atoms within each subunit adopt elongated square pyramidal geometries, classified as a Johnson solid (specifically J_8) (Figure S1).[46] The apex Cu atoms from the pentagonal bases contribute to the fusion, creating a bielongated square pyramidal geometry of 17 Cu atoms, resembling a sand timer with two elongated square pyramids sharing a common base (Figure 2a). However, here each elongated square pyramid geometry shows significant distortion in the arrangement of Cu atoms in the cubic portion (Figure S2). Disordered positioning of the two vertex Cu atoms distorts the four connected facets, resulting in overall structural distortion. The average Cu−Cu distance in the regular facets is 2.6697 ± 0.0153 Å, indicating strong cuprophilic interactions (Figure S3).[43] In contrast, the irregular facets show an increased average distance of 3.1354 ± 0.0694 Å due to disordered arrangements, causing outward displacement of Cu atoms. Detailed analysis shows that the regular facets remain ordered, supported by additional Cu atoms, with one facet forming the pentagonal base. The other facet is stabilized by the attachment of antenna-like Cu_3 units, which form triangular prism-like geometries (Figure 2b). The average distance between the Cu atoms in this antenna-like Cu_3 unit is 2.6572 ± 0.0292 Å, and it maintains an average distance of 2.7117 ± 0.0435 Å from the cubic facet, both indicative of strong cuprophilic interactions. These precise measurements suggest robust interactions that contribute to the structural integrity of the facet. Conversely, the absence of these stabilizing Cu_3 units on the opposite facet results in a lack of structural support, causing the Cu atoms to be arranged in a disordered manner. So, the presence of the Cu_3 units is thus crucial for maintaining the ordered structure and preventing the deformation observed in the absence of these units.

The overall metallic architecture is protected by four hydride atoms, 18 thiolate ligands, and six triphenylphosphine ligands. The hydride atoms are integrated within the metallic framework, attaching specifically to the regular facets of the cubic structures (Figure 2b). These hydrides play a critical role in stabilizing the metallic core by reinforcing the interactions between the Cu atoms, thereby maintaining the integrity of the ordered configuration. The quantitative and qualitative analysis of hydrides is further verified through electrospray ionization mass spectrometry (ESI-MS) and ^1H NMR studies, which will be discussed later. Furthermore, we employed a deep-learning approach based on a convolutional neural network (CNN) to predict hydride-site probabilities using the heavy-atom positions from SCXRD as input.[47] As shown in Figure S4, four sites exhibit nearly 100% occupancy, and their positions, as predicted by the CNN (Figure S4 inset), align with those fixed in the SCXRD data. The 18 thiolate ligands are strategically positioned around the metallic architecture, providing additional stabilization and preventing aggregation by forming a protective layer around the metal atoms. The Cu−S bond lengths range from 2.2183 to 2.4402 Å, with an average of 2.3157 ± 0.0168 Å. The thiolate ligands exhibit specific coordination modes, categorized into four subcategories (Figures 2c and S5). Four thiolate ligands stabilize the fused structural architecture by exhibiting a μ_3 bridging mode, each bridging two Cu atoms from the two elongated square pyramids and another Cu atom from the Cu_3 unit. This attachment restricts the structure to a core−shell configuration, forming a Cu_9 geometry that favors a body-centered cubic architecture. Meanwhile, the other eight thiolate ligands protect the four open faces of each cube within the elongated square pyramid geometry, exhibiting a μ_4 bridging mode and coordinating with the constituent Cu atoms. Another set of four thiolate ligands connects each Cu_3 unit to the elongated square pyramids through a μ_3 bridging mode. The final two thiolate ligands exhibit a μ_2 bridging mode, linking exclusively to the Cu_3 unit. The triphenylphosphine ligands are attached to the outward-oriented Cu atoms (Figure 2d). The Cu−P bond lengths range from 2.2045 to 2.2176 Å, with an average of 2.2113 ± 0.0031 Å. Specifically, four triphenylphosphine units are attached to the four distorted Cu atoms that extend outward from the elongated square pyramid geometry. The remaining two triphenylphosphine units are attached to the Cu_3 units, further stabilizing the structure. The atomic packing is facilitated by efficient intermolecular C−H−π and π−π interactions between the outer surfaces of the protecting ligands (Figure S6). These interactions contribute to the overall stability and robustness of the metallic architecture. Furthermore, the absence of counterions in the unit cell indicates that the Cu_{23} NC is neutral in charge.

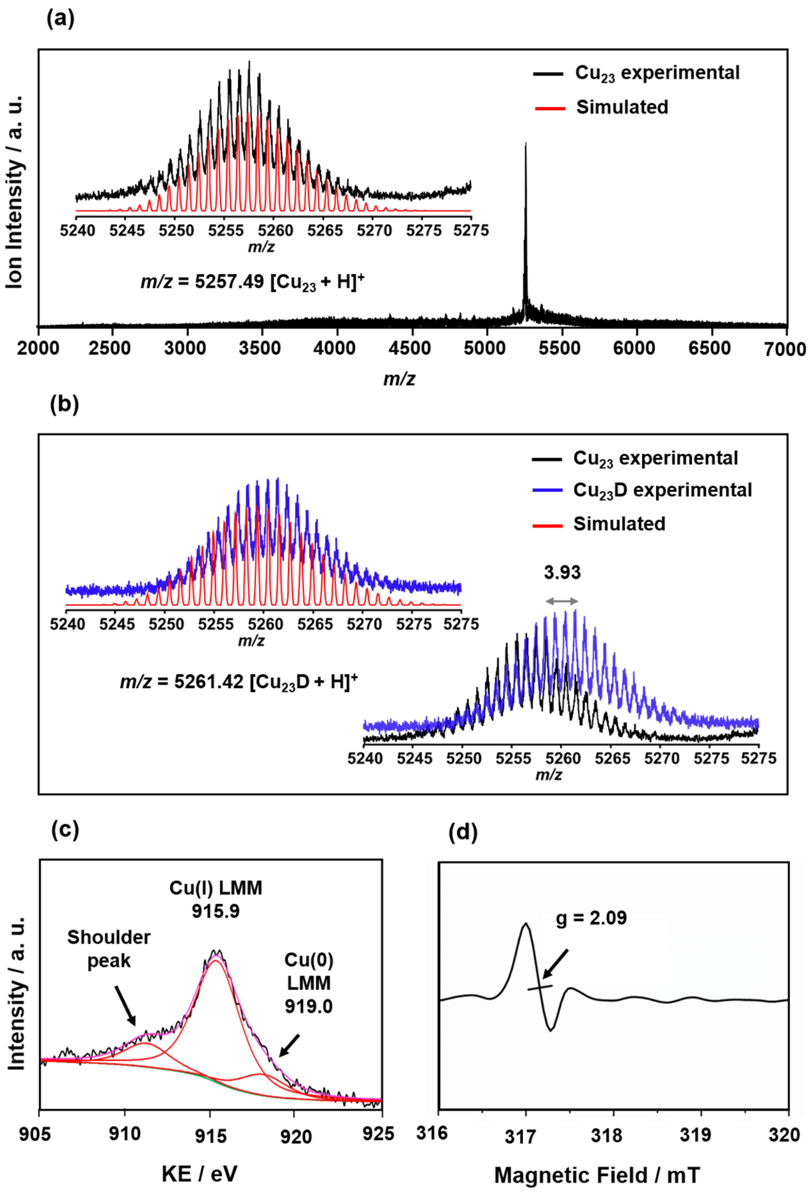

Figure 3. (a) Positive mode ESI mass spectra of Cu_{23} NC. Inset is showing the matching of experimental and simulated peak of Cu_{23} NC. (b) ESI-MS spectra of $Cu_{23}D$ NC and the difference between Cu_{23} NC and $Cu_{23}D$ NC. (c) Deconvoluted Cu LMM XAES spectrum of Cu_{23} NC. (d) EPR spectrum of Cu_{23} NC.

The overall charge state and molecular formula of Cu_{23} NC were further confirmed by ESI-MS. In the positive mode ESI-MS spectrum, a single molecular ion peak was observed at m/z = 5257.49 (Figure 3a). This peak matches exactly with the simulated pattern of $[Cu_{23} + H^+]$, where the isotropic pattern confirms its monocationic charge state, indicating fragmentation during ionization via protonation. Although SCXRD measurements confirmed the number of hydrides, ESI-MS measurements provided additional confirmation of their presence. To gain deeper insights into the source of these hydrides, we utilized $NaBD_4$ as the reducing agent, replacing $NaBH_4$, and synthesized $[Cu_{23}D_4(SC_7H_7)_{18}(PPh_3)_6]$ ($Cu_{23}D$) NC. In the ESI-MS spectrum of this deuterated NC, a peak was observed at m/z = 5261.42 (Figure 3b inset). This peak displayed a prominent upshift of approximately 3.93 m/z compared to the Cu_{23} NC, confirming the successful replacement of hydrides with deuteride atoms. The comparison of ^1H NMR peaks between Cu_{23} and $Cu_{23}D$ NCs reveals the presence of two distinct types of hydrides in the structure (Figure S7).

In the bulk state, the survey spectrum obtained from X-ray photoelectron spectroscopy (XPS) confirms the presence of all constituent elements in Cu_{23} NC (Figure S8). The high-resolution binding energy spectrum further reveals that Cu exists in the +1-oxidation state, while the thiolate ligands are in the −1-oxidation state (Figure S9). Given the neutral charge state of the NC, one Cu atom must be in the 0-oxidation state. However, distinguishing Cu(0) from Cu(I) in the XPS binding energy spectrum is not possible.[45] This differentiation is achieved using X-ray excited Cu LMM auger electron spectroscopy (XAES), which shows peaks at 915.9 and 919.0 eV, corresponding to Cu(I) and Cu(0), respectively, in the Gaussian−Lorentzian band (Figure 3c).[48] An additional Gaussian−Lorentzian band with a peak position at ∼ 911 eV was considered to eliminate the effect of other orbital electrons on the XAES, which appeared as a shoulder peak (Figure 3c).

https://doi.org/10.1021/jacs.5c05665
J. Am. Chem. Soc. 2025, 147, 23733−23742

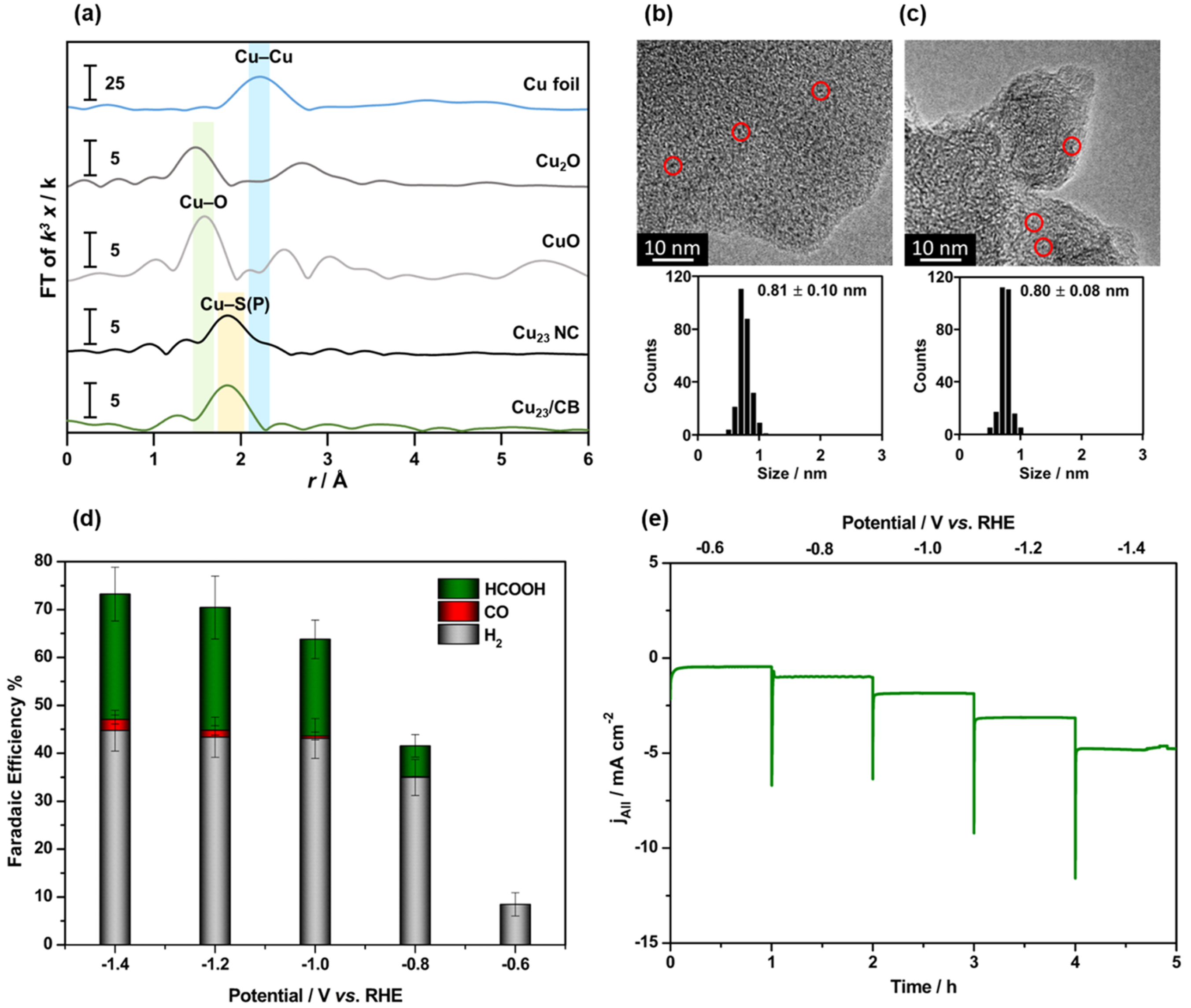

Figure 4. (a) FT-EXAFS spectra comparison of Cu_{23} NC before and after loading on CB, TEM images and the size histogram of (b) only Cu_{23} NC and (c) Cu_{23}/CB, (red circles are directing the NCs) (d) FE for CO_2 reduction products for Cu_{23}/CB at different applied potentials, error bars representing the mean ± standard deviation, $n = 3$, (e) and total current density (j_{All}) for Cu_{23}/CB at different applied potentials.

To further verify the presence of an unpaired electron, electron paramagnetic resonance (EPR) spectroscopy was conducted at 77 K. The EPR spectrum exhibited an isotropic signal with a *g*-value of 2.09 (Figure 3d). This isotropic pattern indicates the symmetric positioning of the Cu(0) atom, suggesting it resides at the fused center, the only symmetric position within the NC unit. Further validation comes from theoretical approximation supporting the presence of the Cu(0) atom at the fused center of the NC by both spin density and partial atomic charge calculation. We have observed the highest spin density and least positive charge for the fused center of the NC (Figure S10).

The Cu_{23} NC exhibits a monotonic decrease in the UV−vis absorbance spectrum in the solvent medium, with a small shoulder band in the ∼ 400−450 nm region, closely matching the simulated spectrum (Figure S11). Further analysis of the absorption band suggests a transition from an orbital localized at the two ends of the cluster to a superatomic 1P-like orbital. However, at room temperature we could not detect any luminescence property of it. In this work, we aim to explore the potential of a uniquely designed Cu_{23} NC as a catalyst for CO_2RR. To perform the electrochemical measurements, a thin film electrode was fabricated using a spray coating technique. This involved depositing a slurry of the Cu_{23} NCs and CB onto a carbon paper substrate (see the details in Supporting Information). It is crucial to maintain the geometric and electronic structure of the NCs during this loading process to preserve their electrocatalytic properties. The stability of the Cu_{23} NCs during this process was assessed using X-ray absorption fine structure (XAFS) spectroscopy. The X-ray absorption near-edge structure (XANES) spectra at the Cu K-edge for both the pristine Cu_{23} NC and the loaded catalysts (Cu_{23}/CB) showed significant overlap, indicating no notable changes in their electronic states (Figure S12). Both samples displayed a peak ∼ 8992 eV, confirming the presence of a mixture of Cu(I) and Cu(0) species, as this peak lies between the characteristic energies of Cu(0) and Cu(I) species. Further insights were gained from the Fourier transform-extended X-

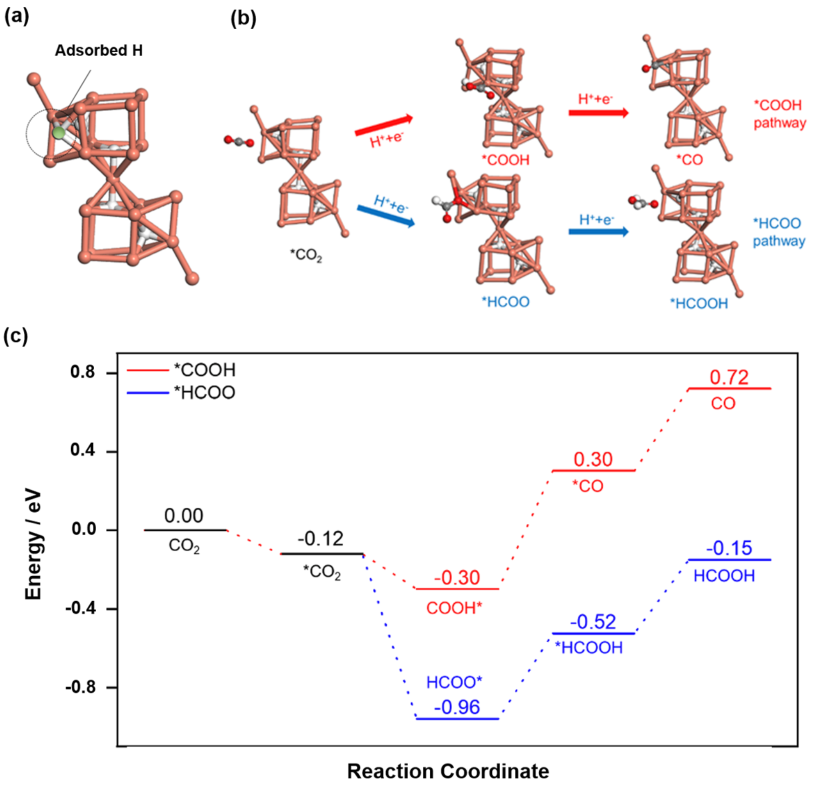

Figure 5. (a) H adsorption at the active site, (b) DFT-optimized adsorption geometries of reactant, intermediate, and product at the active site of the NC where two main pathways are involved, (c) DFT-computed energy profiles of the associated pathways. All the carbon parts and associated hydrogen atoms are removed from the NC for the clarity of the figure. Color legend: Cu, brown; S, yellow; P, violet; O, red; C, gray; H, white.

ray absorption fine structure (FT-EXAFS) spectra at the Cu K-edge. The spectra revealed a similar geometric arrangement in both the pristine and loaded catalysts, with an identical peak observed at ∼ 1.8 Å, which is attributed to Cu−P or Cu−S bonding (Figure 4a). Further transmission electron microscopic (TEM) images confirm the discrete nature of the Cu_{23} NCs and its consistent size even after loading on the CB surface (Figures 4b,c and S13). This consistent structural feature underscores the preservation of the Cu_{23} NC's structural integrity during the electrode fabrication process, crucial for its performance as a CO_2RR catalyst.

The electrochemical performance of Cu_{23}/CB was thoroughly evaluated across a range of constant voltages, specifically from −0.6 to −1.4 V vs. the reversible hydrogen electrode (RHE). This evaluation was conducted using CO_2-saturated 0.1 M $KHCO_3$ aqueous solution as the electrolyte within a gas-flow H-type cell setup. Following the electrochemical testing, an in-depth analysis was performed utilizing gas chromatography (GC) and ^1H NMR to characterize the gas and liquid products, respectively. Our results indicated that hydrogen (H_2), carbon monoxide (CO), and HCOOH were the products generated during the CO_2RR (Figures 4d and S14). To verify that these products originated from the flowing CO_2, a control experiment was carried out using constant-potential electrolysis in an argon (Ar) atmosphere instead of CO_2. The absence of CO_2RR products at all tested potentials in the Ar atmosphere confirmed that the detected products were indeed derived from CO_2 and not from any other source (Figure S15). A control experiment was also conducted on the CB surface without the catalyst as shown in Figure S16. The Faradaic efficiency (FE) data demonstrated a significant increase in total efficiency with increasing potential, rising from 8% at −0.6 V to 74% at −1.4 V (vs. RHE) (Figure 4d) upon introducing the catalyst onto the CB surface. Initially, at −0.6 V, no CO_2RR products were obtained. The formation of HCOOH and a small amount of CO was first observed at −0.8 V (vs. RHE). As the potential became more negative (from −1.0 to −1.4 V vs. RHE), the selectivity for HCOOH increased significantly, reaching saturation (FE_{HCOOH} ∼ 26%) at −1.2 V (vs. RHE), where hydrogen evolution reaction (HER) was nearly at constant. Beyond −1.2 V vs. RHE, the formation of CO increases with more negative potential while the HER and FE_{HCOOH} remain nearly constant. This suggests that, at potentials more negative than −1.2 V vs. RHE, the catalytic surface reaches a steady-state regime for HCOOH and H_2 production, while CO formation continues to be activated or kinetically favored. The product-specific current densities exhibit a corresponding trend, as shown in Figure S17. At −1.2 V vs. RHE, the estimated turnover frequencies (TOFs) provide further insight into the product selectivity and intrinsic catalytic activity for this NC. The TOF for HCOOH formation reaches 113.4 h^{-1}, indicating a significantly higher rate of product generation per active site compared to CO formation, which exhibits a much lower TOF of only 6.54 h^{-1}. This behavior is also reflected in the associated Tafel plots (Figure S18), which illustrate the kinetic response of each product pathway to the applied potential. The Tafel slope for HCOOH is relatively low, indicative of a faster electron transfer or chemical step under moderate overpotentials.

To compare the electrocatalytic performance of Cu_{23} NC, we synthesized Cu nanoparticles (NPs) via a calcination process using a similar precursor salt, yielding an average particle size of ∼ 30 nm, as confirmed by TEM (Figure S19). The electrocatalytic behavior of these Cu NPs was investigated using linear sweep voltammetry (LSV) and cyclic voltammetry (CV), both of which exhibited higher reduction currents compared to Cu_{23} NC (Figure S20). However, FE analysis revealed that these higher reduction currents were mainly due to uncontrolled competing HER (FE_{H2}~80%) at −1.0 V (vs. RHE) (Figure S21). The specificities of FE_{HCOOH} ~ 8% and FE_{CO} ~ 6% for Cu NPs highlight the superior selectivity of Cu_{23} NCs for HCOOH formation. The HCOOH selectivity of Cu_{23} NC was further compared with several other Cu NCs synthesized using a similar Cu precursor salt (Table S2). While a general trend of increased catalytic reactivity with decreasing NC size was observed, the correlation was not entirely linear. This suggests that structural/electronic architecture plays a significant role in determining product selectivity, likely due to its influence on the stabilization of key reaction intermediates.

To evaluate the stability of the material under the applied electrochemical conditions, we identified the constant current densities at each voltage for 1 h duration (Figure 4e). Chronoamperometric measurements were then conducted at −1.0 V (vs. RHE) for a period of 6 h to determine the material's practical applicability (Figure S22). Notably, the current density remained stable over this extended period, showing no discernible degradation. Following this prolonged electrochemical catalysis, we further assessed the stability of the Cu_{23} NCs outside the electrochemical environment after electrocatalysis. TEM images confirmed the structural integrity of the NCs, evidenced by the consistent size of the individual NCs (Figure S23). The Cu K-edge XANES spectra exhibited no significant changes in spectral features compared to those before catalysis, indicating that the electronic structure retains the Cu(I)/Cu(0) configuration (Figure S24). Similarly, the FT-EXAFS spectra for Cu−S(P) bonds suggest that the qualitative coordination environment of Cu remains unchanged (Figure S25). XPS studies further confirm that the oxidation state of the metal atoms is preserved (Figures S26 and S27). However, discrepancies were observed in the P 2p peaks before and after the electrocatalytic reaction, compared to the bare NC (Figure S28). We attribute this to interactions with the conductive substrate, leading to the partial removal of PPh_3 ligands from the NC surface during electrocatalysis. This assumption is supported by Fourier-transform infrared (FT-IR) analysis, which reveals an intense O = P stretching frequency in the postcatalysis sample (Figure S29). Nevertheless, due to the neutral nature of the PPh_3 ligand, the overall electronic structure of the cluster remains unchanged. Thus, this desorption occurs during the electrochemical process, leading to some current loss, which prevents the overall FE from reaching its optimal level.

To gain deeper insight into the mechanistic pathway, we carried out DFT modeling and found that the antenna-like Cu_3 units to both sides of the overall geometry forms hollow, triangular prism-like sites (Figure 2b), which are favorable for H adsorption due to its least hindered position by the nearby S atoms and the associated thiolate groups (E_{ads} = −0.89 eV; Figure 5a) (Figure S30). This aligns with the cluster's preference for HER at low overpotentials. Additionally, we identified this site as the active center for CO_2RR as well (Figure 5b), likely due to the extra partial valences of the associated Cu atoms, making them less positively charged or more reduced (Figure S8). While the central Cu atom is the most reduced, it is buried and inaccessible for direct adsorbate interaction. We investigated the two main CO_2RR pathways on the Cu_{23} NC, leading separately to HCOOH and CO. As shown in Figure 5, the hollow triangular prism-like site is active for CO_2RR, with *COOH and *HCOO preferring adsorption at this location (Figure 5b). The energy profiles (Figure 5c) suggest that the *HCOO pathway is more favorable, showing stronger intermediate adsorption and a lower limiting potential (0.46 eV from *HCOO to *HCOOH vs 0.60 eV from *COOH to *CO). The preference for *HCOO over *COOH can be further explained by the carbonyl oxygen atom in HCOO bridging two more reduced Cu atoms (Figure 5b). These theoretical findings are in strong agreement with experimental observations, reinforcing the conclusion that Cu_{23} NCs exhibit a higher selectivity toward HCOOH formation over CO. Furthermore, to benchmark the CO_2RR efficiency of Cu_{23} NCs against only Cu(I)-based NCs, we conducted a comparative computational analysis with $[Cu_{14}(SR)_3(PR_3)_7H_{10}]^+$ (Cu_{14}) and $[Cu_7(SR)_7(PR_3)_3]$ (Cu_7) NCs (for computational efficiency, -R groups were simplified to -H), both of which also facilitate the reduction of CO_2 to HCOOH.[38,49] Notably, we observed distinct differences in the potential-limiting steps across these NCs, which can be attributed to variations in intermediate stabilization at the catalytic sites. In Cu_{14} and Cu_7 NCs, where Cu(I) exclusively constitutes the whole NC, the potential-limiting step corresponds to the activation of $*CO_2$ to *HCOO (Figure S31) which is also align with the literature.[33] This is due to the weaker interaction of *HCOO with the clusters, leading to a higher activation energy for this step. In contrast, in Cu_{23} NCs, the presence of both Cu(0) and a free electron significantly enhances the stabilization of *HCOO. As a result, the potential-limiting step shifts to the subsequent reduction of *HCOO to *HCOOH. Thus, the favorable electronic and geometric effect in Cu_{23} NCs underscores its critical role in modulating CO_2RR pathways and product selectivity.

CONCLUSIONS

In conclusion, we reported an atomically precise Cu_{23} NC uniquely formed by the integration of two similar Cu(I) subunits through a central Cu(0) atom. This distinct structural architecture, along with the specific arrangement of the protecting ligands, ensures the electronic and geometric stability of the NC despite the presence of a highly reactive Cu(0) center. We leveraged this remarkable stability to evaluate the electrocatalytic properties of the Cu_{23} NC in the CO_2RR when supported on the CB surface. Our results demonstrate that the Cu_{23} NC exhibits selective production of HCOOH, achieving a maximum FE_{HCOOH} of ~ 26% at an applied potential of −1.2 V (vs. RHE). DFT computation explained the selectivity of this specific product through stronger intermediate adsorption and lower limiting potential values on the Cu(0)-containing Cu_{23} NC than on similar-sized Cu(I) NCs. Despite some loss of neutral ligands during the prolonged electrochemical process, the overall stable electronic environment of the metallic architecture underscores the importance of this structural arrangement.

ASSOCIATED CONTENT

Supporting Information

The Supporting Information is available free of charge at https://pubs.acs.org/doi/10.1021/jacs.5c05665.

Experimental section, crystal data and structure refinement parameters, comparison of catalytic activity, geometric analysis of the NC, theoretical analysis for hydride location, NMR, XPS spectrum, charge distribution, UV−vis spectrum and associated transitions, XANES spectrum, raw data for electrocatalytic CO2RR and comparison with inert atmosphere, chronoamperometric measurements with or without catalyst, TEM images, comparative electrocatalytic activities, FT-EXAFS spectra and FT-IR, theoretical understanding of the comparative active catalytic center and effectivity (PDF)

Accession Codes

Deposition Number 2394142 contains the supplementary crystallographic data for this paper. These data can be obtained free of charge via the joint Cambridge Crystallographic Data Centre (CCDC) and Fachinformationszentrum Karlsruhe Access Structures service.

AUTHOR INFORMATION

Corresponding Authors

Tokuhisa Kawawaki − *Research Institute for Science & Technology, Tokyo University of Science, Tokyo 162-8601, Japan; Department of Applied Chemistry, Faculty of Science, Tokyo University of Science, Tokyo 162-8601, Japan; Carbon Value Research Center, Tokyo University of Science, Noda, Chiba 278-8510, Japan;* orcid.org/0000-0003-3282-8964; Email: kawawaki@rs.tus.ac.jp

De-en Jiang − *Department of Chemical and Biomolecular Engineering, Vanderbilt University, Nashville, Tennessee 37235, United States;* orcid.org/0000-0001-5167-0731; Email: de-en.jiang@vanderbilt.edu

Yuichi Negishi − *Carbon Value Research Center, Tokyo University of Science, Noda, Chiba 278-8510, Japan; Institute of Multidisciplinary Research for Advanced Materials, Tohoku University, Sendai 980-8577, Japan;* orcid.org/0000-0003-3965-1399; Email: yuichi.negishi.a8@tohoku.ac.jp

Authors

Sourav Biswas − *Research Institute for Science & Technology, Tokyo University of Science, Tokyo 162-8601, Japan;* orcid.org/0000-0001-9250-5556

Yamato Shingyouchi − *Department of Applied Chemistry, Faculty of Science, Tokyo University of Science, Tokyo 162-8601, Japan*

Maho Kamiyama − *Department of Applied Chemistry, Faculty of Science, Tokyo University of Science, Tokyo 162-8601, Japan*

Masaki Ogami − *Department of Applied Chemistry, Faculty of Science, Tokyo University of Science, Tokyo 162-8601, Japan*

Haohong Song − *Interdisciplinary Materials Science, Vanderbilt University, Nashville, Tennessee 37235, United States;* orcid.org/0009-0003-2037-7905

Bo Li − *Department of Chemical and Biomolecular Engineering, Vanderbilt University, Nashville, Tennessee 37235, United States*

Song Wang − *Hefei National Research Center for Physical Sciences at the Microscale, School of Chemistry and Materials Science, University of Science and Technology of China, Hefei, Anhui 230026, China;* orcid.org/0000-0003-1252-8091

Complete contact information is available at:
https://pubs.acs.org/10.1021/jacs.5c05665

Author Contributions

○S.B. and Y.S. contributed equally to this wok. All authors have given approval to the final version of the manuscript

Notes

The authors declare no competing financial interest.

ACKNOWLEDGMENTS

Y.N. and T.K. acknowledge the financial support of the JSPS KAKENHI (grant no. 24K01459, 23KK0098, 23H00289 and 22K19012), Scientific Research on Innovative Areas “Aquatic Functional Materials” (grant no. 22H04562), the Yazaki Memorial Foundation for Science and Technology, Advanced Technology Institute Research Grants, Takahashi Industrial and Economic Research Foundation, and the Kumagai Foundation for Science and Technology and the Ogasawara Foundation for the Promotion of Science and Engineering. H.S., B.L., and D.J. were supported by the U.S. Department of Energy, Office of Science, Office of Basic Energy Sciences, Chemical Sciences, Geosciences, and Biosciences Division, Catalysis Science Program.

REFERENCES

(1) Jin, R.; Zeng, C.; Zhou, M.; Chen, Y. Atomically Precise Colloidal Metal Nanoclusters and Nanoparticles: Fundamentals and Opportunities. *Chem. Rev.* **2016**, *116*, 10346−10413.

(2) Chakraborty, I.; Pradeep, T. Atomically Precise Clusters of Noble Metals: Emerging Link between Atoms and Nanoparticles. *Chem. Rev.* **2017**, *117*, 8208−8271.

(3) Zou, X.; Kang, X.; Zhu, M. Recent Developments in the Investigation of Driving Forces for Transforming Coinage Metal Nanoclusters. *Chem. Soc. Rev.* **2023**, *52*, 5892−5967.

(4) Jin, Y.; Zhang, C.; Dong, X.-Y.; Zang, S.-Q.; Mak, T. C. Shell Engineering to Achieve Modification and Assembly of Atomically-Precise Silver Clusters. *Chem. Soc. Rev.* **2021**, *50*, 2297−2319.

(5) Biswas, S.; Das, S.; Negishi, Y. Progress and Prospects in the Design of Functional Atomically-Precise Ag(I)-thiolate Nanoclusters and their Assembly Approaches. *Coord. Chem. Rev.* **2023**, *492*, No. 215255.

(6) Hirai, H.; Ito, S.; Takano, S.; Koyasu, K.; Tsukuda, T. Ligand-protected Gold/Silver Superatoms: Current Status and Emerging Trends. *Chem. Sci.* **2020**, *11*, 12233−12248.

(7) Ott, L. S.; Finke, R. G. Transition-metal Nanocluster Stabilization for Catalysis: A Critical Review of Ranking Methods and Putative Stabilizers. *Coord. Chem. Rev.* **2007**, *251*, 1075−1100.

(8) Cook, A. W.; Hayton, T. W. Case Studies in Nanocluster Synthesis and Characterization: Challenges and Opportunities. *Acc. Chem. Res.* **2018**, *51*, 2456−2464.

(9) Baghdasaryan, A.; Bürgi, T. Copper Nanoclusters: Designed Synthesis, Structural Diversity, and Multiplatform Applications. *Nanoscale* **2021**, *13*, 6283−6340.

(10) Biswas, S.; Negishi, Y. Exploring the Impact of Various Reducing Agents on Cu Nanocluster Synthesis. *Dalton Trans.* **2024**, *53*, 9657−9663.

(11) Biswas, S.; Das, S.; Negishi, Y. Advances in Cu Nanocluster Catalyst Design: Recent Progress and Promising Applications. *Nanoscale Horiz.* **2023**, *8*, 1509−1522.

(12) Liu, Y.; Yu, J.; Lun, Y.; Wang, Y.; Wang, Y.; Song, S. Ligand Design in Atomically Precise Copper Nanoclusters and Their Application in Electrocatalytic Reactions. *Adv. Funct. Mater.* **2023**, *33*, No. 2304184.

(13) Liu, X.; Astruc, D. Atomically Precise Copper Nanoclusters and their Applications. *Coord. Chem. Rev.* **2018**, *359*, 112−126.

(14) Cook, A. W.; Jones, Z. R.; Wu, G.; Scott, S. L.; Hayton, T. W. An Organometallic Cu_{20} Nanocluster: Synthesis, Characterization, Immobilization on Silica, and “Click” Chemistry. *J. Am. Chem. Soc.* **2018**, *140*, 394−400.

(15) Dong, C.; Huang, R. W.; Sagadevan, A.; Yuan, P.; Gutiérrez-Arzaluz, L.; Ghosh, A.; Nematulloev, S.; Alamer, B.; Mohammed, O. F.; Hussain, I.; Rueping, M.; Bakr, O. M. Isostructural Nanocluster Manipulation Reveals Pivotal Role of One Surface Atom in Click Chemistry. *Angew. Chem., Int. Ed.* **2023**, *62*, No. e202307140.

(16) Das, A. K.; Biswas, S.; Pal, A.; Manna, S. S.; Sardar, A.; Mondal, P. K.; Sahoo, B.; Pathak, B.; Mandal, S. A Thiolated Copper-hydride Nanocluster with Chloride Bridging as a Catalyst for Carbonylative C−N Coupling of Aryl Amines under Mild Conditions: A Combined Experimental and Theoretical study. *Nanoscale* **2024**, *16*, 3583−3590.

(17) Sagadevan, A.; Ghosh, A.; Maity, P.; Mohammed, O. F.; Bakr, O. M.; Rueping, M. Visible-light Copper Nanocluster Catalysis for the C−N Coupling of Aryl Chlorides at Room Temperature. *J. Am. Chem. Soc.* **2022**, *144*, 12052−12061.

(18) Nematulloev, S.; Sagadevan, A.; Alamer, B.; Shkurenko, A.; Huang, R.; Yin, J.; Dong, C.; Yuan, P.; Yorov, K. E.; Karluk, A. A.; Mir, J. W.; Hasanov, E. B.; Hedhili, M. N.; Halappa, N. M.; Eddaoudi, M.; Mohammed, O. F.; Rueping, M.; Bakr, M. O. Atomically Precise Defective Copper Nanocluster Catalysts for Highly Selective C−C Cross-Coupling Reactions. *Angew. Chem., Int. Ed.* **2023**, *62*, No. e202303572.

(19) Bodiuzzaman, M.; Murugesan, K.; Yuan, P.; Maity, B.; Sagadevan, A.; Malenahalli H, N.; Wang, S.; Maity, P.; Alotaibi, M. F.; De-en, J.; Abulikemu, M.; Mohammed, O. F.; Cavallo, L.; Rueping, M.; Bakr, O. M. Modulating Decarboxylative Oxidation Photocatalysis by Ligand Engineering of Atomically Precise Copper Nanoclusters. *J. Am. Chem. Soc.* **2024**, *146*, 26994−27005.

(20) Kawawaki, T.; Okada, T.; Hirayama, D.; Negishi, Y. Atomically Precise Metal Nanoclusters as Catalysts for Electrocatalytic CO_2 Reduction. *Green Chem.* **2024**, *26*, 122−163.

(21) Ma, Y.; Sun, M.; Xu, H.; Zhang, Q.; Lv, J.; Guo, W.; Hao, F.; Cui, W.; Wang, Y.; Yin, J.; Wen, H.; Lu, P.; Wang, G.; Zhou, J.; Yu, J.; Ye, C.; Gan, L.; Zhang, D.; Chu, S.; Gu, L.; Shao, M.; Huang, B.; Fan, Z. Site-selective Growth of fcc-2H-fcc Copper on Unconventional Phase Metal Nanomaterials for Highly Efficient Tandem CO_2 Electroreduction. *Adv. Mater.* **2024**, *36*, No. 2402979.

(22) Wang, J.; Sun, M.; Xu, H.; Hao, F.; Wa, Q.; Su, J.; Zhou, J.; Wang, Y.; Yu, J.; Zhang, P.; Ye, R.; Chu, S.; Huang, B.; Shao, M.; Fan, Z. Coordination Environment Engineering of Metal Centers in Coordination Polymers for Selective Carbon Dioxide Electroreduction toward Multicarbon Products. *ACS Nano* **2024**, *18*, 7192−7203.

(23) Guo, L.; Zhou, J.; Liu, F.; Meng, X.; Ma, Y.; Hao, F.; Xiong, Y.; Fan, Z. Electronic Structure Design of Transition Metal-Based Catalysts for Electrochemical Carbon Dioxide Reduction. *ACS Nano* **2024**, *18*, 9823−9851.

(24) Wang, D.; Wang, J.; Wang, Z.; Zhang, N.; Zeng, J.; Zhong, H.; Zhang, X. Supported Cu/Ni Bimetallic Cluster Electrocatalysts Boost CO_2 Reduction. *Precision Chem.* **2024**, *2*, 96−102.

(25) Du, Y.; Sheng, H.; Astruc, D.; Zhu, M. Atomically Precise Noble Metal Nanoclusters as Efficient Catalysts: a Bridge between Structure and Properties. *Chem. Rev.* **2020**, *120*, 526−622.

(26) Kawawaki, T.; Okada, T.; Takemae, K.; Tomihari, S.; Negishi, Y. Size-Dependent Carbon Dioxide Reduction Activity of Copper Nanoparticle and Nanocluster Electrocatalysts. *ChemNanoMat* **2024**, *10*, No. e202300575.

(27) Yang, D.; Wang, J.; Wang, Q.; Yuan, Z.; Dai, Y.; Zhou, C.; Wan, X.; Zhang, Q.; Yang, Y. Electrocatalytic CO_2 Reduction Over Atomically Precise Metal Nanoclusters Protected by Organic Ligands. *ACS Nano* **2022**, *16*, 15681−15704.

(28) Kwak, K.; Lee, D. Electrochemistry of Atomically Precise Metal Nanoclusters. *Acc. Chem. Res.* **2019**, *52*, 12−22.

(29) Yuan, X.; Zhu, M. Recent Advances in Atomically Precise Metal Nanoclusters for Electrocatalytic Applications. *Inorg. Chem. Front.* **2023**, *10*, 3995−4007.

(30) Biswas, S.; Shingyouchi, Y.; Ogami, M.; Kamiyama, M.; Kawawaki, T.; Negishi, Y. Advancing Electrochemical CO_2 Reduction with group 11 Metal Nanoclusters for Renewable Energy Solutions. *EcoEnergy* **2024**, *2*, 400−418.

(31) Mu, W.-L.; Li, L.; Cong, X.-Z.; Chen, X.; Xia, P.; Liu, Q.; Wang, L.; Yan, J.; Liu, C. Hierarchical Assembly of High-Nuclearity Copper(I) Alkynide Nanoclusters: Highly Effective CO_2 Electroreduction Catalyst toward Hydrocarbons. *J. Am. Chem. Soc.* **2024**, *146*, 28131−28140.

(32) Guan, A.; Yang, C.; Wang, Q.; Qian, L.; Cao, J.; Zhang, L.; Wu, L.; Zheng, G. Atomic-Level Copper Sites for Selective CO2 Electroreduction to Hydrocarbon. *ACS Sustainable Chem. Eng.* **2021**, *9*, 13536−13544.

(33) Liu, L. J.; Wang, Z. Y.; Wang, Z. Y.; Wang, R.; Zang, S. Q.; Mak, T. C. Mediating CO_2 Electroreduction Activity and Selectivity Over Atomically Precise Copper Clusters. *Angew. Chem., Int. Ed.* **2022**, *61*, No. e202205626.

(34) Han, H.; Yao, Y.; Bhargava, A.; Wei, Z.; Tang, Z.; Suntivich, J.; Voznyy, O.; Robinson, R. D. Tertiary Hierarchical Complexity in Assemblies of Sulfur-bridged Metal Chiral Clusters. *J. Am. Chem. Soc.* **2020**, *142*, 14495−14503.

(35) Wu, Q. J.; Si, D. H.; Sun, P. P.; Dong, Y. L.; Zheng, S.; Chen, Q.; Ye, S. H.; Sun, D.; Cao, R.; Huang, Y. B. Atomically Precise Copper Nanoclusters for Highly Efficient Electroreduction of CO_2 towards Hydrocarbons via Breaking the Coordination Symmetry of Cu Site. *Angew. Chem., Int. Ed.* **2023**, *62*, No. e202306822.

(36) Zhang, L.; Li, X.-X.; Lang, Z.-L.; Liu, Y.; Liu, J.; Yuan, L.; Lu, W.-Y.; Xia, Y.-S.; Dong, L.-Z.; Yuan, D.-Q.; Lan, Y.-Q. Enhanced Cuprophilic Interactions in Crystalline Catalysts Facilitate the Highly Selective Electroreduction of CO_2 to CH_4. *J. Am. Chem. Soc.* **2021**, *143*, 3808−3816.

(37) Weal, G. R.; Guomundsson, K. I.; Mackenzie, F. D.; Whiting, J. R.; Smith, N. B.; Skúlason, E.; Garden, A. L. Calculations of the Effect of Catalyst Size and Structure on the Electrocatalytic Reduction of CO_2 on Cu Nanoclusters. *Nanoscale* **2024**, *16*, 5242−5256.

(38) Shingyouchi, Y.; Ogami, M.; Biswas, S.; Tanaka, T.; Kamiyama, M.; Ikeda, K.; Hossain, S.; Yoshigoe, Y.; Osborn, D. J.; Metha, G. F.; et al. Ligand-Dependent Intracluster Interactions in Electrochemical CO_2 Reduction Using Cu_{14} Nanoclusters. *Small* **2025**, *21*, No. 2409910.

(39) Tang, Q.; Lee, Y.; Li, D.-Y.; Choi, W.; Liu, C.; Lee, D.; Jiang, D.-e. Lattice-hydride Mechanism in Electrocatalytic CO_2 Reduction by Structurally Precise Copper-hydride Nanoclusters. *J. Am. Chem. Soc.* **2017**, *139*, 9728−9736.

(40) Li, F.; Tang, Q. The Critical Role of Hydride (H^-) Ligands in Electrocatalytic CO_2 Reduction to HCOOH by $[Cu_{25}H_{22}(PH_3)_{12}]Cl$ Nanocluster. *J. Catal.* **2020**, *387*, 95−101.

(41) Li, S.; Yan, X.; Tang, J.; Cao, D.; Sun, X.; Tian, G.; Tang, X.; Guo, H.; Wu, Q.; Sun, J.; He, J.; Shen, H. Cu_{26} Nanoclusters with Quintuple Ligand Shells for CO_2 Electrocatalytic Reduction. *Chem. Mater.* **2023**, *35*, 6123−6132.

(42) Biswas, S.; Tanaka, T.; Song, H.; Ogami, M.; Shingyouchi, Y.; Hossian, S.; Kamiyama, M.; Kosaka, T.; Nakatani, R.; Niihori, Y.; et al. Highly Selective Methanol Synthesis Using Electrochemical CO_2 Reduction with Defect-Engineered Cu_{58} Nanoclusters. *Small Sci.* **2025**, *5*, No. 2400465.

(43) Das, A. K.; Biswas, S.; Wani, V. S.; Nair, A. S.; Pathak, B.; Mandal, S. $Cu_{18}H_3(S\text{-}Adm)_{12}(PPh_3)_4Cl_2]$: Fusion of Platonic and Johnson Solids through a Cu(0) Center and Its Photophysical Properties. *Chem. Sci.* **2022**, *13*, 7616−7625.

(44) Han, B.-L.; Liu, Z.; Feng, L.; Wang, Z.; Gupta, R. K.; Aikens, C. M.; Tung, C.-H.; Sun, D. Polymorphism in Atomically Precise Cu_{23} Nanocluster Incorporating Tetrahedral $[Cu_4]^0$ Kernel. *J. Am. Chem. Soc.* **2020**, *142*, 5834−5841.

(45) Ghosh, A.; Huang, R.-W.; Alamer, B.; Abou-Hamad, E.; Hedhili, M. N.; Mohammed, O. F.; Bakr, O. M. [Cu61(StBu)-26S6Cl6H14]+: A Core−Shell Superatom Nanocluster with a Quasi-J36 Cu19 Core and an "18-Crown-6" Metal-Sulfide-like Stabilizing Belt. *ACS Mater. Lett.* **2019**, *1*, 297−302.

(46) Johnson, N. W. Convex Polyhedra with Regular Faces. *Can. J. Math.* **1966**, *18*, 169−200.

(47) Wang, S.; Wu, Z.; Dai, S.; Jiang, D.-e. Deep Learning Accelerated Determination of Hydride Locations in Metal Nanoclusters. *Angew. Chem., Int. Ed.* **2021**, *60*, 12289−12292.

(48) Wang, A.; Zhang, M.; Yin, H.; Liu, S.; Liu, M.; Hu, T. Direct Reaction between Silicon and Methanol Over Cu-based Catalysts: Investigation of Active Species and Regeneration of CuCl Catalyst. *RSC Adv.* **2018**, *8*, 19317−19325.

(49) Biswas, S.; Pal, A.; Jena, M. K.; Hossain, S.; Sakai, J.; Das, S.; Sahoo, B.; Pathak, B.; Negishi, Y. Luminescent Hydride-Free [$Cu_7(SC_5H_9)_7(PPh_3)_3$] Nanocluster: Facilitating Highly Selective C−C Bond Formation. *J. Am. Chem. Soc.* **2024**, *146*, 20937−20944.